

## Plasmonic properties of nonstoichiometric zirconium nitride, oxynitride thin films, and their bilayer structures

Qian Guo , Tianrun Wang , Yuehong Ren , Yujing Ran , Chang Gao , Huiping Lu , Zhaotan Jiang , and Zhi Wang \*

*School of Physics, Beijing Institute of Technology, Beijing 100081, People's Republic of China*



(Received 4 January 2021; accepted 19 April 2021; published 16 June 2021)

Nonstoichiometric  $ZrN_x$  (ZrN) thin films,  $ZrO_xN_y$  (ZrON) thin films, and bilayer ZrN/ZrON structures were prepared, and the effects of stoichiometry and interface on their plasmonic properties were investigated. We find that the samples are all B1 structured with similar lattice constants. Higher nitrogen and oxygen content can reduce the screened plasma frequency  $\omega_c$ . Interestingly, the bilayer ZrN/ZrON structures with some ZrON thickness are more metallic than ZrN films, which should be reasonable since the mutual diffusion through the ZrN/ZrON interface may cause a ZrON buffer zone with substitute oxygen atoms generating more free carriers. The postulation is further confirmed by the calculations about the band structure, which indicates that substitute oxygen atoms can depress the interband transition level and cause more carriers in conduction band. This work implies that oxygen substitution is an effective method to enhance the performances of nitride-based plasmonic materials and devices.

DOI: [10.1103/PhysRevMaterials.5.065201](https://doi.org/10.1103/PhysRevMaterials.5.065201)

### I. INTRODUCTION

As optoelectronic components and devices approach nanoscale, controlling the nanodimensional interaction between light and matter has become a major technological challenge for the diffraction limit [1–3]. Surface plasmons are collective charge oscillations based on interaction between electromagnetic radiation and conduction electrons at metallic interfaces or in small metallic nanostructures, leading to an enhanced optical near field. Surface plasmons can realize the manipulation and control of photons at the deep sub-wavelength scale [1,2], and have promised breakthroughs in many technological divisions, such as microelectronics [4], energy harvesting [5], photodetection [6,7], optical information storage [8], and telecommunications [9]. Since the 1990s, the study on the surface plasmons and their applications has sprung up. Initially, only noble metals, such as gold and silver, were used as plasmonic materials because of their high chemical stability and excellent plasma performance in the visible and near-infrared regions [10–12]. However, the application of noble metals is limited by their complementary metal-oxide-semiconductor (CMOS) incompatibility, thermal instability, limited tunability, and excessive loss in visible and near-infrared regions [12–16]. The requirements for the diversity of the plasmonic materials are now recognized, for the purpose of integrating with semiconductor technology and extending the plasma resonance spectral range [12].

Recently, transition-metal nitrides (TMNs), especially  $TiN_x$ , were considered as potential alternative plasmonic materials in the visible and near-infrared spectral range [17–19] because of their excellent plasmonic properties, CMOS compatibility, and high tunability [20–22]. TMNs are

nonstoichiometric compounds, and their carrier concentration largely depends on their N content [23,24]. So, their electronic and optical properties can be easily modulated by nitrogen content. TMNs can form the solid solution of ternary nitrides by element doping to get higher tunability, which has been recently reported in various ternary nitrides with improved plasmonic properties [20,25–27]. It can be expected that oxygen doping is also an effective method to tune the optical properties of TMNs. In fact, it is reported that oxygen doping has a significant impact on the dielectric properties of the  $TiN_x$  [28–30]. The roles of chemical phase and defect types of oxygen-doped samples in tailoring the plasmonic nitride are novel and important issues in plasmonics.

In comparison with  $TiN_x$ , the most extensively studied plasmonic nitride [19,31–34],  $ZrN_x$  is viewed as a viable candidate for photonics and plasmonics [23]. However, the experimental works on plasmonic  $ZrN_x$  are still rare [23,24,35]. In this work,  $ZrN_x$  (ZrN),  $ZrO_xN_y$  (ZrON) thin films, and ZrN/ZrON bilayer structures were fabricated by magnetron sputtering. The effects of nitrogen content, oxygen content, and ZrN/ZrON interface on the plasmonic characteristics of the samples were systematically analyzed. Possibly, the doping manners of oxygen atoms can underly the results. The first-principles calculation of the electronic structure was used and it is confirmed that substitute oxygen atoms can generate more carriers and enhance the metallicity of oxygen-doped films. The results indicate that oxygen substitution is an effective method to improve the plasmonic quality of nitride, and the tunable range of the plasmonic properties of B1-structured TMNs can be extended by oxygen doping.

### II. MATERIALS AND METHODS

ZrN, ZrON thin films, and bilayer ZrN/ZrON structures were prepared by magnetron sputtering. The background

\*wangzhi@bit.edu.cn

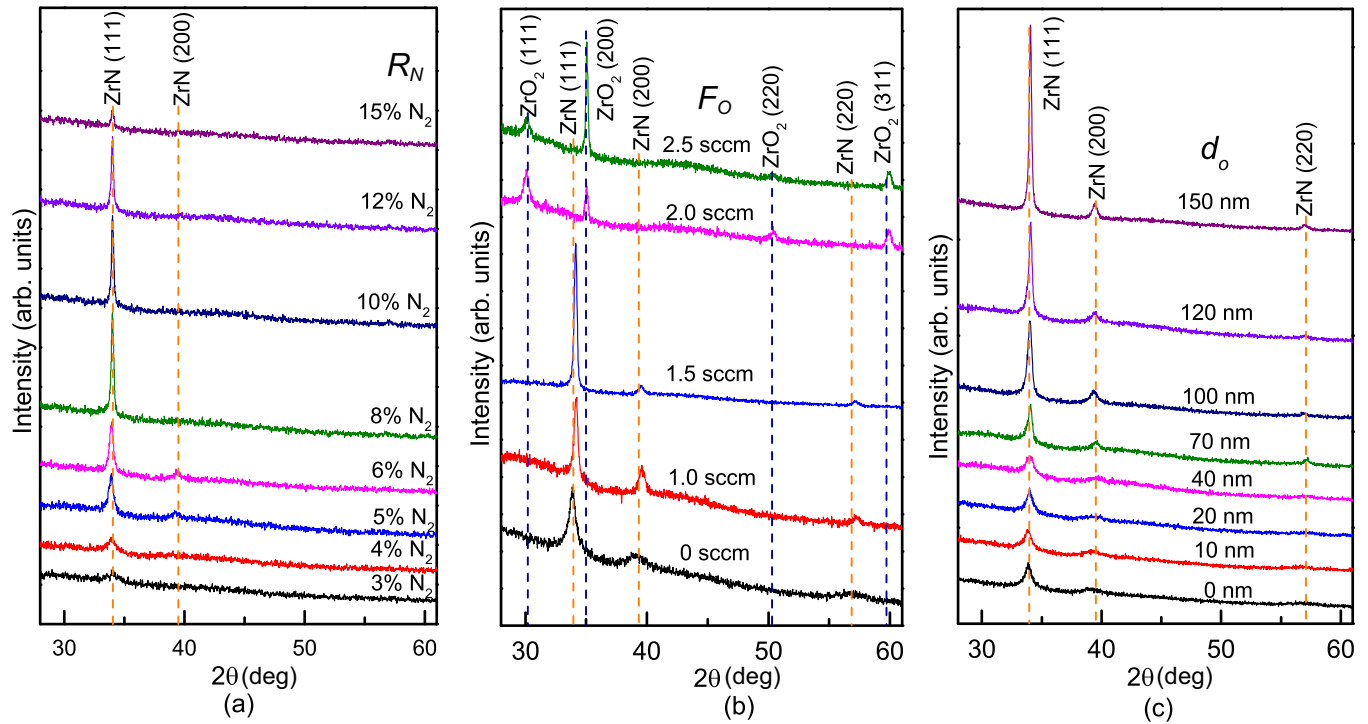


FIG. 1. XRD  $\theta$ - $2\theta$  patterns of the ZrN films (a), ZrON films (b), and bilayer ZrN/ZrON structures (c). The ZrN films were prepared with different flow rate ratio of nitrogen gas  $R_N$ ; the ZrON films were prepared with different oxygen flow rate  $F_O$  ( $R_N = 4\%$ ); the thickness of ZrON layer  $d_o$  of the bilayer ZrN/ZrON structures is different, but their total thickness is the same (150 nm). In the preparation of ZrN/ZrON structures,  $R_N = 4\%$  and  $F_O = 1.5$  sccm.

pressure of the vacuum chamber reached  $8.0 \times 10^{-4}$  Pa, and the working pressure was kept at 0.5 Pa. The metal atoms were dc sputtered with a power 150 W from a 99.9% pure Zr target and deposited on JGS1 SiO<sub>2</sub> substrates and reacted with nitrogen and/or oxygen gas. The films were deposited at room temperature.

For the deposition of ZrN films, N<sub>2</sub> and Ar gas with different flow rates were supplied into the sputtering chamber, with the total flow rate of Ar and N<sub>2</sub> kept stable at 50 sccm. The flow rate ratio of nitrogen gas  $R_N$  was set to 3%, 4%, 5%, 6%, 8%, 10%, 12%, and 15%, respectively. During the deposition of ZrON films, O<sub>2</sub>, N<sub>2</sub>, and Ar were introduced, and  $R_N$  was kept at 4%. The oxygen content of the films was modulated by adjusting the oxygen flow rate  $F_O$ , which was set at 1.0, 1.5, 2.0, and 2.5 sccm, respectively. For the monolayer ZrN and ZrON films, the deposition time is different to get similar thickness of 150 nm. A quartz oscillator was used to control the thickness of the films. During the preparation of bilayer ZrN/ZrON structures, ZrN layers were deposited with  $R_N = 4\%$  on ZrON layer, which were deposited with  $R_N = 4\%$  and  $F_O = 1.5$  sccm. The total thickness of all the bilayer structures is 150 nm, while the thickness of ZrON layers  $d_o$  was adjusted and set at 0, 10, 20, 40, 70, 100, 120, and 150 nm, respectively. The  $d_o$  of 0 and 150 nm correspond to monolayer ZrN and ZrON films, respectively.

The crystal structure of the film was characterized by an x-ray diffraction (XRD) system (Bruker D8 Advance) with Cu- $K\alpha_1$  radiation ( $\lambda = 0.15406$  nm). In order to get the chemical bonding of the samples, a hemispherical optoelectronic analyzer (Thermo Scientific Escalab 250Xi) with

aluminum and magnesium as standard dual anode x-ray photoelectron spectroscopy (XPS). Before XPS characterization, all sample surfaces were etched by 2000 eV argon ion for 5 s. The cross section of the samples was analyzed by a Zeiss Supra 55 scanning electron microscope (SEM). The dielectric function was measured by an ellipsometry (Sentech SE 850 DUV) with a spectral incidence angle of 70°. The measured ellipsometry data were fitted to the Drude-Lorentz model. The film thickness was 150 ( $\pm 20$ ) nm, and the thickness was obtained by an XP-1 surface profilometer of AMBIOS. All characterization tools were performed at room temperature.

The electronic band structures and density of states (DOS) of the stoichiometric fcc-structured ZrN and ZrO<sub>0.5</sub>N<sub>0.5</sub> were calculated within the generalized gradient approximation of Perdew-Burke-Ernzerhof (GGA-PBE) using the CASTEP module in the Materials Studio. The calculations were based on a crystal cell of B1-structured ZrN and ZrO<sub>0.5</sub>N<sub>0.5</sub>. All lattice constants and other parameters were optimized and tested. The cutoff energy was set to be 400 eV and the  $\kappa$ -point set was  $6 \times 6 \times 6$ . The SCF (self consistent field) tolerance was  $1.0 \times 10^{-6}$  eV/atom. The Fermi level is set at zero.

### III. RESULTS AND DISCUSSION

#### A. Structures

Figure 1 shows the XRD patterns of the samples. The analysis of the XRD data was based on JCPDS cards (Nos. 35-0753 and 89-9069). Figure 1(a) shows the XRD patterns of ZrN films prepared with different  $R_N$ . Only fcc-structured ZrN

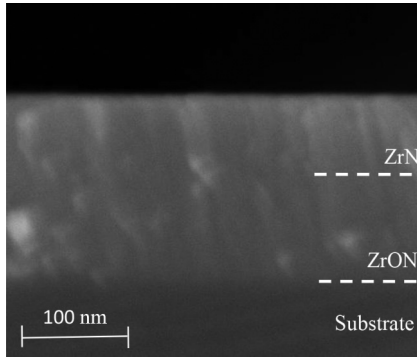


FIG. 2. Cross-sectional SEM image of the bilayer ZrN/ZrON structure with  $d_o = 100$  nm. The dotted line indicates the estimated interface.

characteristic peaks appear. The (111) peak exists in all films, and the (200) peak exists in some films. Obviously, the growth of (111)-oriented grains is preferred under the experimental condition. In addition, the peak intensity of the films with higher and lower  $R_N$  is relatively weaker than that of the films deposited with  $R_N$  from 5% to 12% because too low or too high N content will produce much more nonstoichiometric defects and reduce the crystallinity of the films.

The XRD patterns of the ZrON films deposited with different  $F_O$  are shown in Fig. 1(b). The results show that the diffraction peaks of the films deposited with lower  $F_O$  (1.0 and 1.5 sccm) exhibit similar crystal structure to those of undoped ZrN films. Since the diffraction peaks of stoichiometric fcc-ZrO (111) and stoichiometric fcc-ZrN (111) are very close to each other, this fcc-ZrON phase can be understood as solid solution of rocksalt-structured ZrN and ZrO, in which fcc-ZrN crystallites with O atoms substituting some of the N atoms, with a certain degree of homogeneity. As  $F_O$  increases, the (111) peak of the ZrON films shifts to large-angle direction, which reflects that more and more interstitial oxygen atoms exist in this solid solution with oxygen content increasing. As the  $F_O$  further increases, ZrO<sub>2</sub> phases dominate the samples, which means for higher  $F_O$  (2.0 and 2.5 sccm), the corresponding films are nitrogen-doped zirconium dioxide.

Figure 1(c) shows the XRD results of the bilayer ZrN/ZrON structures with different ZrON layer thickness  $d_o$  and the same total thickness. All the characteristic diffraction peaks are near those of fcc-ZrN. So, the oxynitride layer is also in a structure of solid solution of fcc-ZrO and fcc-ZrN, and the oxygen atoms exist as point defects, such as substitutes and interstitial. The peak intensity of the bilayer samples is comparable to that of monolayer samples in Figs. 1(a) and 1(b). Because the ZrN and ZrON layers have the same crystal structure and close lattice constants, the interfaces have not depressed the crystallinity of the films, as indicated in Fig. 1(c).

The XRD results show the ZrON films with lower oxygen content and ZrN films have the same fcc structure and (111) alignment with close lattice constant. It can be expected that in the ZrN/ZrON bilayer structures the ZrN layer is homoepitaxial on the ZrON layer. Figure 2 indicates the SEM cross-sectional image of the bilayer structure film with  $d_o = 100$  nm. A thin film can be clearly observed on the substrate.

The film has a columnar characteristic, as previously observed in the ZrN films and ZrON films with low oxygen content in Ref. [36]. However, the ZrN/ZrON interface is difficult to find in the SEM image. Maybe there is no abrupt interface because mutual diffusion between the two layers results in an inconspicuous interface. The same crystal structure and close lattice constants of ZrN and ZrON films make the mutual diffusion easy to realize.

## B. XPS

The chemical bonding of the ZrON films was characterized with XPS. Figure 3 shows the N 1s, O 1s, and Zr 3d photoelectron energy regions of ZrON films with different  $F_O$ . Figure 3(a) presents the N 1s XPS spectrum of the ZrON films. There are two peaks, among which the one near 395.4 eV can be assigned to the Zr-N component, and the other near 396.5 eV is O-Zr-N component [37–40]. The O-Zr-N component means the existence of oxygen substitutes. Compared to the ZrN<sub>x</sub> film ( $F_O = 0$  sccm), the O-Zr-N component increases significantly with increasing  $F_O$ , but decreases in the films with  $F_O$  of 2.0 and 2.5 sccm, possibly because much more oxygen interstitial was generated by high  $F_O$ . Figure 3(b) shows the O 1s XPS spectra. There are two components, namely, the ZrO<sub>2</sub> component at 530 eV [41,42] and N-O/O-H component at 532 eV, which are associated to oxidation and adsorbed oxygen atoms on the surface [43,44].

The XPS spectra of the Zr 3d are shown in Fig. 3(c). The ZrO<sub>2</sub> peak was decomposed into two doublets, Zr 3d<sub>5/2</sub> and Zr 3d<sub>3/2</sub> [43,45], which are located near 181.9 and 184.3 eV, respectively. In the XPS spectra of our samples, the peak near 179.1 eV is attributed to the ZrN<sub>x</sub> component [39,45,46]. The ZrN<sub>x</sub> component decreases with increasing  $F_O$ , and disappears when  $F_O$  is greater than 1.5 sccm. The binding energy of ZrO<sub>x</sub>N<sub>y</sub> component is slightly lower than that of ZrO<sub>2</sub> component, and is difficult to detect in Zr 3d spectra. Maybe the shift of the ZrO<sub>2</sub> peak to the lower binding energy is caused by the increase of the ZrO<sub>x</sub>N<sub>y</sub> component in the lower  $F_O$  films. The ZrO<sub>2</sub> peaks in XPS results are partly due to the surface oxidation and absorption after deposition.

The XPS results indicate that the films with low oxygen content ( $F_O = 1.0, 1.5$  sccm) are doped with oxygen substitutions, for the O-Zr-N component increasing with  $F_O$ . However, in these films with low oxygen content there are also some oxygen interstitial, as indicated by the ZrO<sub>2</sub> components in Figs. 3(b) and 3(c). The close interstitial and substitutions constitute ZrO<sub>2</sub> bonds. The ZrO<sub>2</sub> crystal grains are small and difficult to detect by XRD, so there are no ZrO<sub>2</sub> phases in the XRD results of the films with  $F_O = 1.0$  and 1.5 sccm. ZrO<sub>2</sub> phases form in the films with high oxygen content ( $F_O = 2.0$  and 2.5 sccm), which can be confirmed by XRD and XPS results.

Figure 4 shows the N 1s XPS spectrum of the bilayer ZrN/ZrON structures with different ZrON layer thickness  $d_o$ . As mentioned above, there are Zr-N and O-Zr-N components. The increase of  $d_o$  leads to the decrease of Zr-N component because of the reduced thickness of ZrN layer. The O-Zr-N component is enhanced by increasing  $d_o$ . Considering the limitation of the penetration depth of x ray, one possible

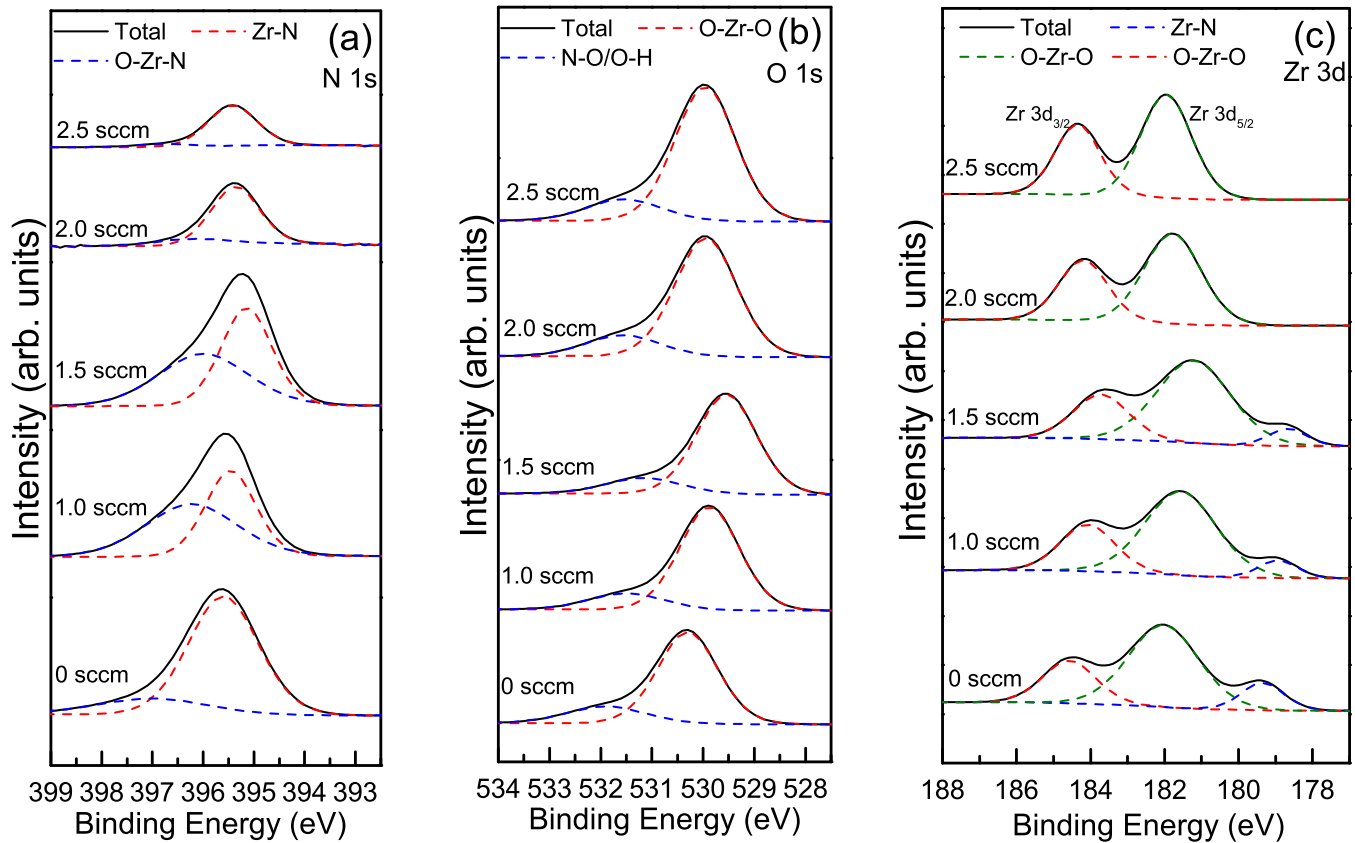


FIG. 3. N 1s (a), O 1s (b), and Zr 3d (c) XPS spectra of ZrON films prepared with different oxygen flow rate  $F_O$  ( $R_N = 4\%$ ).

reason for the increasing of O-Zr-N signals is the mutual diffusion between ZrN and ZrON layers. The oxygen can cross the interface and diffuse into the ZrN layer with a considerable depth. As  $d_o$  increases, the oxygen atoms that diffuse from the ZrON layer are closer to the top surface and are easily detected. Therefore, the O-Zr-N components become stronger with increasing  $d_o$ . The XPS results of the bilayer structure in Fig. 4 are consistent with the XRD result in Fig. 1(c).

### C. Dielectric function

Figure 5 depicts the real part  $\epsilon_1$  and the imaginary part  $\epsilon_2$  of the complex permittivities of the ZrN films of different  $R_N$ .  $\epsilon_1$  and  $\epsilon_2$  were calculated by  $\epsilon_1 = n_0^2 - k^2$  and  $\epsilon_2 = 2n_0k$ , where  $n_0$  and  $k$  are refractive index and extinction coefficient obtained by the ellipsometry. The measured ellipsometric data were fitted to the Drude-Lorentz model [23,47]. The positive and negative  $\epsilon_1$  mean the dielectric and metallic properties of the corresponding samples. It can be seen in Fig. 5(a) that with  $R_N$  increasing, the metallicity of the films gradually decreases. For the films of 3% to 8%  $R_N$ ,  $\epsilon_1$  turns from positive to negative as the wavelength increases, and turns positive again for the films of 5%, 6%, and 8%  $R_N$ . The frequency  $\omega_c$ , at which  $\epsilon_1$  crosses zero, is interpreted as a screened plasmon frequency because a fraction of the total valence electrons is effectively screened [48]. Since  $\omega_c$  is directly proportional to plasma frequency  $\omega_p$ , and  $\omega_p$  is proportional to the square root of carrier concentration [49],  $\omega_c$  reflects the carrier

concentration. The result proves that higher  $R_N$  leads to lower carrier concentration because as  $R_N$  increases, more and more free electrons in the conduction band of the metal are absorbed by the increasing nitrogen atoms. The films deposited with  $R_N$  of 10% to 15% are dielectric in the entire measurement wavelength range since there is little carrier in the conduction bands.

The imaginary part  $\epsilon_2$ , shown in Fig. 5(b), decreases with increasing  $R_N$  at the same  $\lambda$  value. Because the carrier concentration decreases with increasing  $R_N$ , the films deposited with higher  $R_N$  exhibit less metallic and more dielectric. There is a peak in the  $\epsilon_2$  spectra between 200–300 nm, which is related to interband transition [17]. Since  $\epsilon_2$  is recognized to be associated with optical loss [19,24,29], the results of  $\epsilon_2$  indicate that higher nitrogen leads to less optical loss in visible and near infrared.

The  $\epsilon_1$  and  $\epsilon_2$  of ZrON films are shown in Fig. 6. The film deposited with  $F_O$  of 1.0 sccm exhibits similar permittivity behaviors to the undoped ZrN film. The  $\epsilon_1$  of the films turn negative in long-wavelength range. The film deposited with  $F_O$  of 1.5 sccm shows a double epsilon-near-zero characteristic, as the oxygen-doped  $\text{TiN}_x$  films behave in Ref. [28]. The films with  $F_O$  of 2.0 and 2.5 sccm are dielectric in the entire measurement wavelength range because the dominant phases of the films are  $\text{ZrO}_2$  related. A interesting result is that the absolute values of the negative  $\epsilon_1$  are higher than those of the undoped ZrN film in the long-wavelength range, which means the film is more metallic. The results of  $\epsilon_2$  also give the same conclusions as those of  $\epsilon_1$  do.

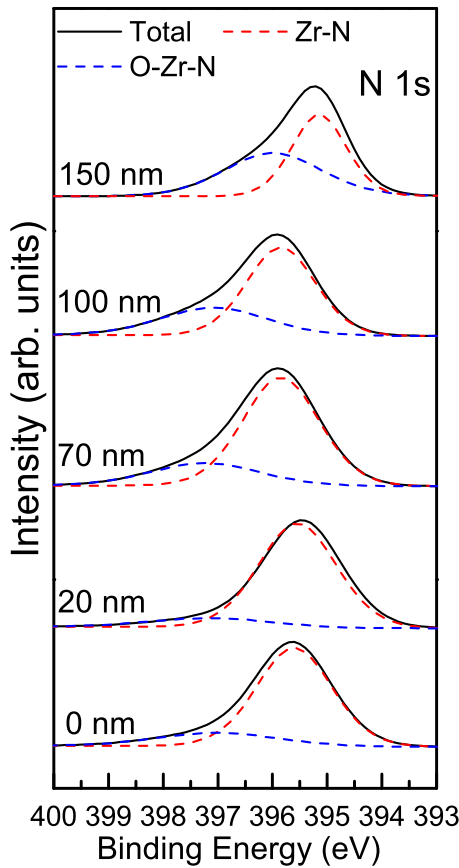


FIG. 4. N 1s XPS spectra of the bilayer ZrN/ZrON structures with different ZrON layer thickness  $d_o$ .

Possibly the specific doping manner, such as oxygen substitute and interstitial, is a crucial microscopically affecting factor leading to the permittivity behavior of ZrON films. For the ZrON film with  $F_O$  of 1.0 sccm, there are more substitute oxygen atoms. A substitute oxygen atom absorbs less electrons of metal than a nitrogen one does, so substitute oxygen doping can lead to more carriers. Higher oxygen content in an oxynitride phase means more oxygen interstitial, which absorbs much more free carrier and makes the films less metallic, as happened in the ZrON film deposited with  $F_O$  of 1.5 sccm. Higher oxygen content caused the formation of  $ZrO_2$  phases, and the films with  $F_O$  of 2.0 and 2.5 sccm turn dielectric.

The dielectric functions of the bilayer ZrN/ZrON structures are shown in Fig. 7. The  $\epsilon_1$  spectra in Fig. 7(a) show that all the curves of bilayer structures do not lie between those of monolayer ZrN and ZrON films. As the oxynitride thickness increases, the  $\hbar\omega_c$  initially increases and reaches its maximum at 70 nm, and then decreases, as shown in the inset of Fig. 7. The monolayer ZrON film ( $d_o = 150$  nm) exhibits a dual epsilon-near-zero characteristic. It is surprising that the bilayer structures with some thickness are more metallic than both monolayer ZrN and ZrON films. A similar conclusion can be drawn from the results of  $\epsilon_2$  shown in Fig. 7(b).

Furthermore, the result indicates that the carrier concentration of bilayer ZrN/ZrON structures is even higher than that of monolayer ZrN film, although the carrier concentration of

monolayer ZrON film is much lower. As mentioned above, the specific doping manner leads to the permittivity behavior of ZrON films. In the bilayer ZrN/ZrON structures, the doping manner is also an important factor affecting the dielectric properties. Furthermore, the doping manner is modulated by the ZrN/ZrON interface. The oxygen atoms of the ZrON layer and the nitrogen atoms of the ZrN layer can mutually diffuse through the interface, and finally form a buffer zone on both sides of the interface with some thickness. The mutual diffusion is easy to realize because ZrON and ZrN layers have the same B1 structure with very close lattice constants, as discussed above. The XPS result in Fig. 4 seems to indicate the mutual diffusion. The buffer zone can be regarded as ZrN doped with low oxygen content, and oxygen atoms exist mainly as substitutes which can lead to more carriers and higher  $\omega_c$ . In the ZrON layer outside the buffer zone, oxygen atoms exist mainly as interstitial which absorb much more free electrons and result in lower carrier concentration.

The thickness of buffer zone varies with the thickness of ZrON layer. When the thickness of oxynitride layer is below 70 nm, the buffer zone possibly covers the whole ZrON layer. The whole ZrON layer and part of ZrN layer are oxynitride with substitute doping oxygen atoms. The thicker the ZrON layer, the thicker the buffer zone, and the more metallic the samples. When the thickness of ZrON layer is above 100 nm, the buffer zone cannot cover the whole ZrON layer, and a zone with more interstitial doping oxygen atoms is left in the bottom of the ZrON layer. The interstitial oxygen atoms reduce the carrier concentration and  $\hbar\omega_c$  of the samples.

#### D. Electronic band structure

Based on the above discussion, it can be seen that substitute oxygen plays an important role in modulating the plasmonic characteristics of ZrON. The affecting mechanism of substitute oxygen can be investigated by the electronic states. The electronic band structures and density of states (DOS) of the stoichiometric fcc-structured ZrN and  $ZrO_{0.5}N_{0.5}$  are calculated by GGA-PBE using the CASTEP module in the Materials Studio software. The calculation was based on a crystal cell as shown in Fig. 8, in which we can see the distances between the atoms are reduced by the oxygen substitution. In  $ZrO_{0.5}N_{0.5}$  crystal cell, oxygen atoms substitute 50% of nitrogen atoms at their sites. The density of states is given by [50]

$$D(E) = \frac{2}{(2\pi)^3} \sum_n \int \delta(E - \epsilon_{nk}) d^3\mathbf{k}, \quad (1)$$

where  $\epsilon_{nk}$  is single-electron energy. The calculation of the electronic band structure is based on the Kohn-Sham single-electron equation [51,52]

$$\left[ -\frac{1}{2} \nabla^2 + V_{\text{ext}}(\mathbf{r}) + V_H(\mathbf{r}) + V_{xc}(\mathbf{r}) \right] \psi_i(\mathbf{r}) = \epsilon_i \psi_i(\mathbf{r}), \quad (2)$$

where  $V_{\text{ext}}(\mathbf{r})$ ,  $V_H(\mathbf{r})$ , and  $V_{xc}(\mathbf{r})$  represent the potential due to the nuclei, the Hartree potential, and the exchange-correlation potential.

The calculated electronic structures and DOS are shown in Fig. 9. In the figure, we can see there are three separate bundles of energy bands in the energy range of to 10 eV, and each bundle comes from a single ionic contribution and

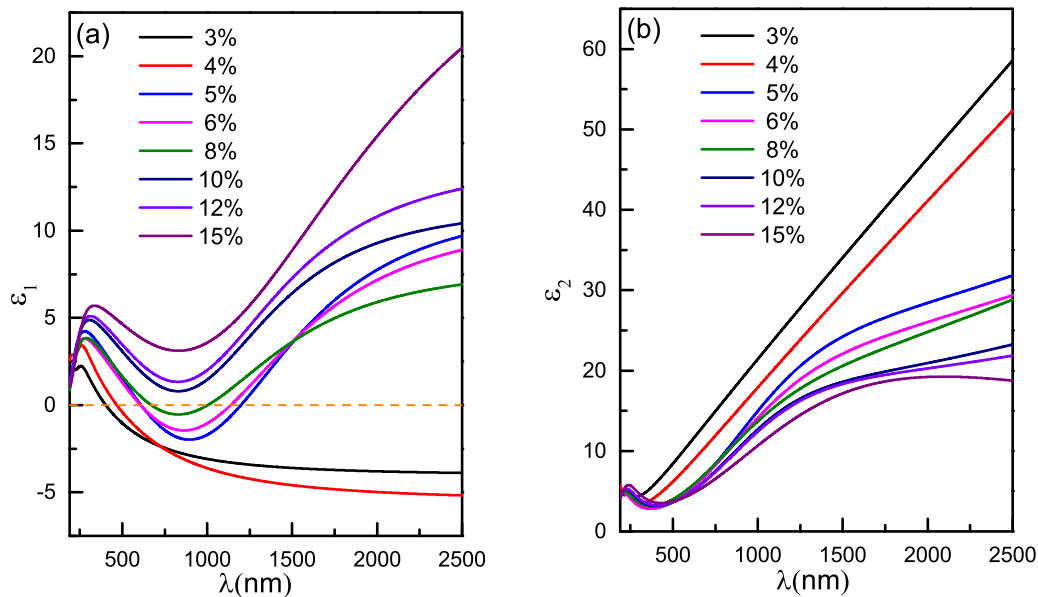


FIG. 5. Real part  $\epsilon_1$  (a) and imaginary part  $\epsilon_2$  (b) of the permittivities of the ZrN films deposited with different nitrogen flow rate ratio  $R_N$ .

a minor covalent contribution [48]. At the bottom, around  $-15$  eV, the bands with low dispersion are mainly built of the nonmetal N  $2s$  and O  $2s$  states. This bundle of bands is similar for ZrN and  $ZrO_{0.5}N_{0.5}$  because N  $2s$  level and O  $2s$  level are close to each other. Just below the Fermi level, there are overlapping bands which originate mainly from the nonmetal  $2p$ , and contain also appreciable Zr  $4d$  state. The bundle of energy bands located near the Fermi level (from  $-2$  to  $6$  eV) derives mostly from Zr  $4d$  state.

For metal nitride, plasmon resonance excitation is mainly due to the interaction between interband and intraband transitions. The bands around the Fermi level in Fig. 9 are responsible for the metallicity (negative  $\epsilon_1$ ) in the long-wavelength range. For energy from  $-2$  to  $0$  eV, the only

possible excitations of the valence electrons are due to intra-band transition in Zr  $4d$  bands crossing the Fermi level [48]. In this region, the partial coupling of the N  $2p$  (O  $2p$ ) states contributes little to absorption. At higher energy, interband transition from nonmetal  $2p$  to Zr  $4d$  will create a dielectric screening, which makes  $\epsilon_1$  change from negative to positive at  $\omega_c$ . Above  $\omega_c$ , the interband transition will make  $\epsilon_1$  a small positive value.

According to the selection rules of photonic excitation, interband transition is that the nonmetal  $2p$  electrons ( $-9$  to  $-2$  eV) are excited to the Fermi level. There are three characteristic energy levels in the nonmetal  $2p$  bands, which are marked in the DOS function in Fig. 9. For ZrN, at  $E_1$  the total DOS reaches its minimum, and the nonmetal N  $2p$  state begins

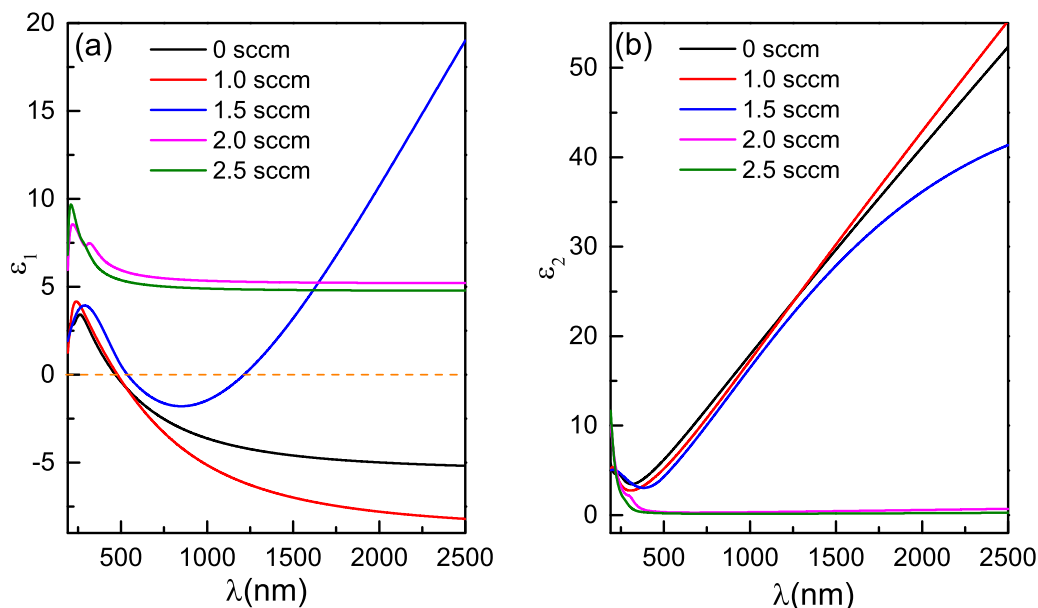


FIG. 6. Real part  $\epsilon_1$  (a) and imaginary part  $\epsilon_2$  (b) of the permittivities of the ZrON films deposited with different oxygen flow rate  $F_O$ .

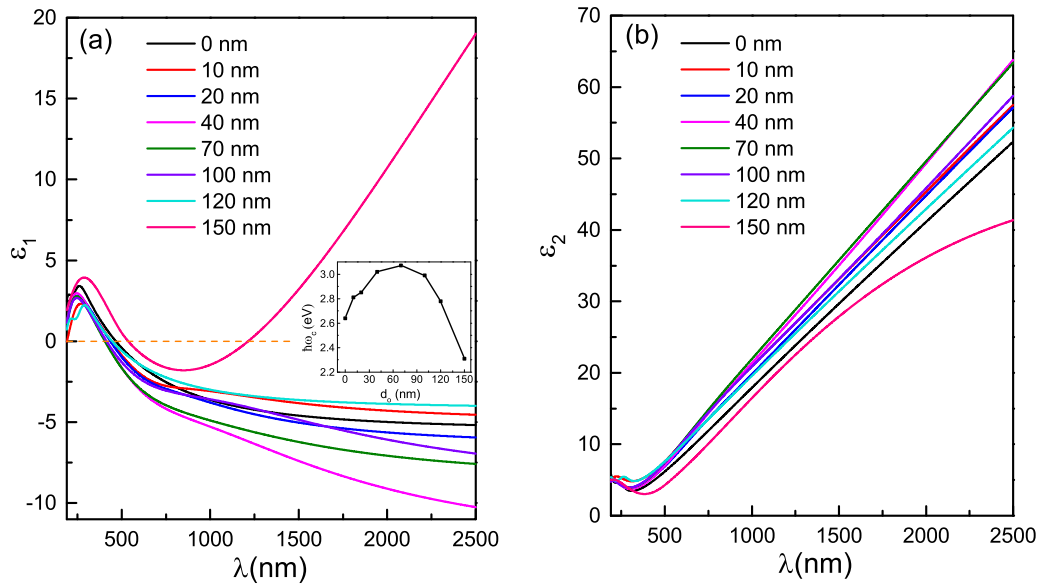


FIG. 7. Real part  $\epsilon_1$  (a) and imaginary part  $\epsilon_2$  (b) of the permittivities of the bilayer Zr/ZrON structures with different ZrON layer thickness  $d_0$ . The inset shows the  $\hbar\omega_c$  as a function of  $d_0$ . The thicknesses of 0 and 150 nm correspond to monolayer ZrN and ZrON films, respectively.

to dominate the DOS function. So  $E_1$  can be regarded as the threshold energy of the dielectric contribution to the optical response because the value of  $E_1$  is approximately equal to the  $\hbar\omega_1$  value of film with 4%  $R_N$ , shown in Fig. 5(a). At about 3.7 and 5.0 eV below  $E_F$ , there are the local maximum and the global maximum of the DOS of N 2p bands, which are marked as  $E_2$  and  $E_3$  respectively. The maximum of DOS means the maximum of the intensity of the interband transition. Possibly,  $E_2$  and  $E_3$  are related to the maximum of positive  $\epsilon_1$  and  $\epsilon_2$ .

For the convenience of comparison, the total DOS of ZrN and  $ZrO_{0.5}N_{0.5}$  are shown together in Fig. 10. Obviously, the influence of oxygen doping is mainly on the nonmetal 2p bands and Zr 4d bands (from -8 to 0 eV). Because O 2p level is deeper than N 2p level, oxygen substitution makes the 2p bands of the ZrN shift away from the Fermi energy level. The characteristic energy levels  $E_1, E_2, E_3$  of ZrN are also made lower to  $E'_1, E'_2, E'_3$  for  $ZrO_{0.5}N_{0.5}$ . The integrals of a DOS function from  $E'_1$  (or  $E_1$ ) to Fermi level, as shown in Fig. 9, indicate that the  $ZrO_{0.5}N_{0.5}$  has more carriers in

the conduction band. Both the shift of characteristic levels and the variation of carrier concentration confirm that oxygen substitution to nitrogen makes fcc-ZrN more metallic.

#### IV. CONCLUSIONS

ZrN and ZrON films with different nitrogen and oxygen content were prepared by magnetron sputtering, and their bilayer ZrN/ZrON structures with different ZrON layer thickness were also prepared and studied. The ZrN films, the ZrON films with low oxygen content, and the bilayer structures exhibit a rocksalt structure and a preferred (111) orientation. Large oxygen flow can lead to the formation of  $ZrO_2$  phases in the ZrON films. For the ZrN thin films, higher  $R_N$  can reduce the screened plasma frequency  $\omega_c$  and the optical loss of the samples. For ZrON films, higher oxygen content causes interstitial defects and makes the films dielectric, while lower oxygen content generated oxygen substitutes and enhances the screened plasma frequency of the ZrON films. The bilayer

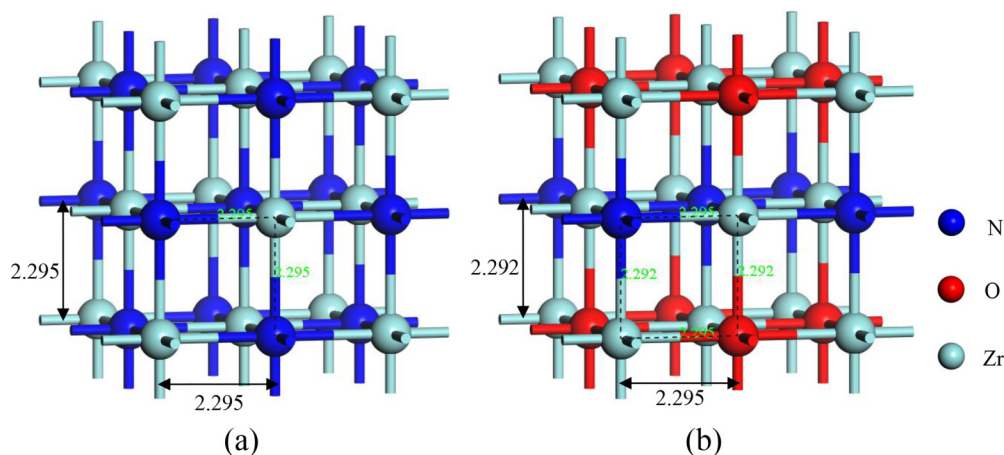


FIG. 8. Crystal cells of stoichiometric ZrN (a) and  $ZrO_{0.5}N_{0.5}$  (b).

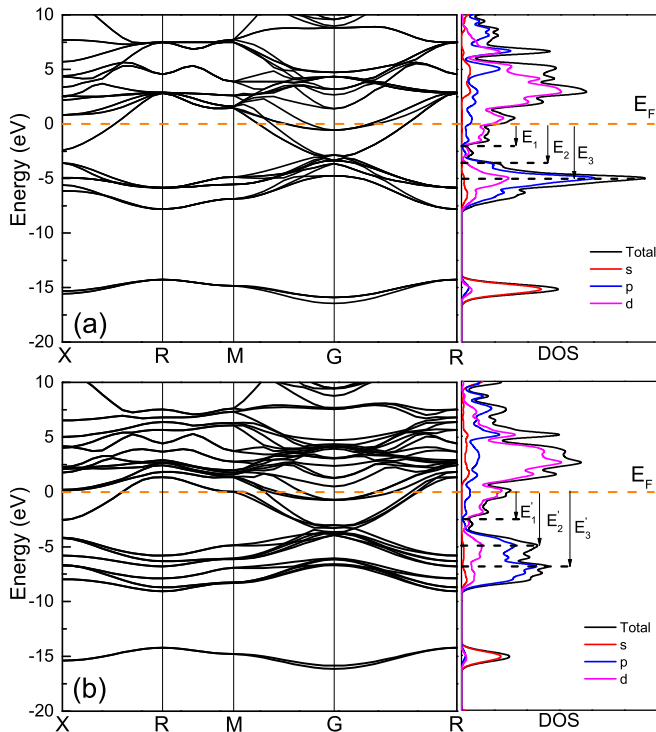


FIG. 9. Electronic band structures and the density of states of ZrN (a) and ZrO<sub>0.5</sub>N<sub>0.5</sub> (b).

ZrN/ZrON structures with some ZrON thickness are even more metallic than ZrN films, possibly because the mutual diffusion through the ZrN/ZrON interface causes a ZrON buffer zone with substitute oxygen atoms. The modification of the plasmonic properties of the samples is microscopically related

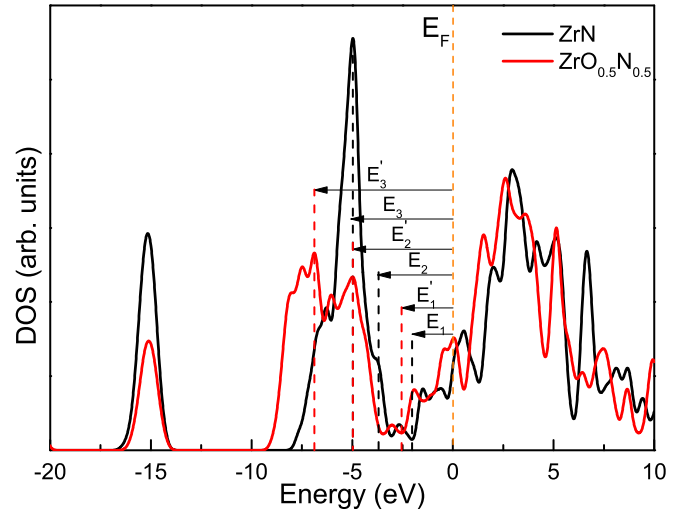


FIG. 10. The density of states of ZrN and ZrO<sub>0.5</sub>N<sub>0.5</sub>.

to the specific doping manner, which is confirmed by the first-principles calculations about the band structure and the DOS. The calculations indicate that oxygen substitutes cause more carriers in conduction band and make ZrN film more metallic. This study implies that the quality of nitride-based plasmonic materials and devices can be further enhanced by oxygen substitution to nitrogen atoms.

#### ACKNOWLEDGMENTS

This work was supported by the National Natural Science Foundation of China (Grants No. 11774029 and No. 51002010). We thank L. Zhao of National Center for Nanoscience and Technology for the ellipsometry measurement.

- [1] V. Giannini, A. I. Fernández-Domínguez, S. C. Heck, and S. A. Maier, *Chem. Rev.* **111**, 3888 (2011).
- [2] W. L. Barnes, A. Dereux, and T. W. Ebbesen, *Nature (London)* **424**, 824 (2003).
- [3] L. Piatkowski, N. Accanto, and N. F. van Hulst, *ACS Photon.* **3**, 1401 (2016).
- [4] M. T. Sheldon, J. van De Groep, A. M. Brown, A. Polman, and H. A. Atwater, *Science* **346**, 828 (2014).
- [5] Q. Gan, F. J. Bartoli, and Z. H. Kafafi, *Adv. Mater.* **25**, 2385 (2013).
- [6] M. Oshita, H. Takahashi, Y. Ajiki, and T. Kan, *ACS Photon.* **7**, 673 (2020).
- [7] H. Chalabi, D. Schoen, and M. L. Brongersma, *Nano Lett.* **14**, 1374 (2014).
- [8] K. Kumar, H. Duan, R. S. Hegde, S. C. W. Koh, J. N. Wei, and J. K. W. Yang, *Nat. Nanotechnol.* **7**, 557 (2012).
- [9] S. P. Burgos, H. W. Lee, E. Feigenbaum, R. M. Briggs, and H. A. Atwater, *Nano Lett.* **14**, 3284 (2014).
- [10] J. A. Schuller, E. S. Barnard, W. Cai, Y. C. Jun, J. S. White, and M. L. Brongersma, *Nat. Mater.* **9**, 193 (2010).
- [11] Y. C. Jun, R. D. Kekatpure, J. S. White, and M. L. Brongersma, *Phys. Rev. B* **78**, 153111 (2008).
- [12] G. V. Naik, V. M. Shalaev, and A. Boltasseva, *Adv. Mater.* **25**, 3264 (2013).
- [13] U. Guler, V. M. Shalaev, and A. Boltasseva, *Mater. Today* **18**, 227 (2015).
- [14] R. Ji, B. X. Xu, Z. H. Cen, J. F. Ying, and Y. T. Toh, *J. Appl. Phys.* **117**, 17A918 (2015).
- [15] A. Boltasseva, *MRS Bull.* **39**, 461 (2014).
- [16] Y. Chen, M. Lee, and C. Wang, *Japan. J. Appl. Phys.* **53**, 08MG02 (2014).
- [17] P. Patsalas, *Thin Solid Films* **688**, 137438 (2019).
- [18] L. Zhang, S. Tong, H. Liu, Y. Li, and Z. Wang, *Mater. Lett.* **171**, 304 (2016).
- [19] L. Zhang, H. Liu, X. Suo, S. Tong, Y. Li, Z. Jiang, and Z. Wang, *Mater. Lett.* **185**, 295 (2016).

- [20] C. Metaxa, S. Kassavetis, J. F. Pierson, D. Gall, and P. Patsalas, *ACS Appl. Mater. Interfaces* **9**, 10825 (2017).
- [21] M. Kumar, N. Umezawa, S. Ishii, and T. Nagao, *ACS Photon.* **3**, 43 (2016).
- [22] A. Catellani, P. D'Amico, and A. Calzolari, *Phys. Rev. Mater.* **4**, 015201 (2020).
- [23] P. Patsalas, N. Kalfagiannis, and S. Kassavetis, *Materials* **8**, 3128 (2015).
- [24] H. Lu, Y. Ran, S. Zhao, L. Jia, C. Gao, Q. Guo, Z. Jiang, F. Yang, and Z. Wang, *J. Phys. D: Appl. Phys.* **52**, 245102 (2019).
- [25] S. Kassavetis, D. V. Bellas, G. Abadias, E. Lidorikis, and P. Patsalas, *Appl. Phys. Lett.* **108**, 263110 (2016).
- [26] Y. Ran, H. Lu, S. Zhao, L. Jia, Q. Guo, C. Gao, Z. Jiang, and Z. Wang, *Appl. Surf. Sci.* **476**, 560 (2019).
- [27] H. Lu, Y. Ran, S. Zhao, Q. Guo, C. Gao, Z. Jiang, F. Yang, and Z. Wang, *Appl. Surf. Sci.* **505**, 144579 (2020).
- [28] L. Braic, N. Vasilantonakis, A. Mihai, I. J. V. Garcia, S. Fearn, B. Zou, N. M. Alford, B. Doiron, R. F. Oulton, S. A. Maier, A. V. Zayats, and P. K. Petrov, *ACS Appl. Mater. Interfaces* **9**, 29857 (2017).
- [29] L. Jia, H. Lu, Y. Ran, S. Zhao, H. Liu, Y. Li, Z. Jiang, and Z. Wang, *J. Mater. Sci.* **54**, 1452 (2019).
- [30] H. Iwataa, H. Ishii, D. Kato, S. Kawashima, K. Kodama, M. Furusawa, M. Tanaka, and T. Sekiya, *J. Vac. Sci. Technol. A* **36**, 061509 (2018).
- [31] J. Hu, X. Ren, A. N. Reed, T. Reese, D. Rhee, B. Howe, L. J. Lauhon, A. M. Urbas, and T. W. Odom, *ACS Photon.* **4**, 606 (2017).
- [32] H. Reddy, U. Guler, Z. Kudyshev, A. V. Kildishev, V. M. Shalaev, and A. Boltasseva, *ACS Photon.* **4**, 1413 (2017).
- [33] D. Shah, A. Catellani, H. Reddy, N. Kinsey, V. Shalaev, A. Boltasseva, and A. Calzolari, *ACS Photon.* **5**, 2816 (2018).
- [34] L. Zhang, H. Liu, X. Suo, S. Tong, Y. Li, Z. Jiang, and Z. Wang, *J. Mater. Sci.* **52**, 6442 (2017).
- [35] R. Kamakura, S. Murai, K. Fujita, and K. Tanaka, *ACS Photon.* **5**, 3057 (2018).
- [36] J. Huang, K. Chang, and G. Yu, *Surf. Coat. Technol.* **201**, 6404 (2007).
- [37] I. Milosev, H. H. Strehblow, M. Gaberscek, and B. Navinsek, *Surf. Interfaces Anal.* **24**, 448 (1996).
- [38] M. Del Re, R. Gouttebaron, J. P. Dauchot, P. Leclere, G. Terwagne, and M. Hecq, *Surf. Coat. Technol.* **174**, 240 (2003).
- [39] Y. Cheng and Y. F. Zheng, *IEEE Trans. Plasma Sci.* **34**, 1105 (2006).
- [40] L. I. Johansson and H. I. P. Johansson, *Mater. Sci. Forum* **325**, 335 (2000).
- [41] E. Portolan, C. L. G. Amorim, G. V. Soares, C. Aguzzoli, C. A. Perottoni, I. J. R. Baumvol, and C. A. Figueroa, *Thin Solid Films* **517**, 6493 (2009).
- [42] I. Valov, R. A. de Souza, C. Z. Wang, A. Borger, C. Korte, M. Martin, K.-D. Becker, and J. Janek, *J. Mater. Sci.* **42**, 1931 (2007).
- [43] H. Wiame, M. A. Centeno, S. Picard, P. Bastians, and P. Grange, *J. Eur. Ceram. Soc.* **18**, 1293 (1998).
- [44] D. Roman, J. Bernardi, C. L. G. D. Amorim, F. S. D. Souza, and R. L. O. Basso, *Mater. Chem. Phys.* **130**, 147 (2011).
- [45] T. Muneshwar and K. Cadien, *Appl. Surf. Sci.* **435**, 367 (2018).
- [46] P. Prieto, L. Galán, and J. M. Sanz, *Phys. Rev. B* **47**, 1613 (1993).
- [47] M. Popović, M. Novaković, E. Schmidt, P. Schöppe, N. Bibić, C. Ronning, and Z. Rakoević, *Opt. Mater.* **72**, 775 (2017).
- [48] A. Catellani and A. Calzolari, *Phys. Rev. B* **95**, 115145 (2017).
- [49] G. V. Naik, J. Kim, and A. Boltasseva, *Opt. Mater. Expr.* **1**, 1090 (2011).
- [50] N. W. Ashcroft and N. D. Mermin, *Solid State Physics* (Holt, Rinehart and Winston, New York, 1976).
- [51] W. Kohn and L. Sham, *Phys. Rev.* **140**, A1133 (1965).
- [52] V. Milman, B. Winkler, J. A. White, C. J. Pickard, M. C. Payne, E. V. Akhmatkaya, and R. H. Nobes, *Int. J. Quantum Chem.* **77**, 895 (2000).